Sea level changes can trigger earthquake sequences in a hydrothermal system near Istanbul

P. Martínez-Garzón[1], G. C. Beroza[2], G. M. Bocchini[3] and M. Bohnhoff[1,4]

[1] Helmholtz Centre Potsdam GFZ German Research Centre for Geosciences, Section 4.2 Geomechanics and Scientific Drilling, Potsdam, Germany.

[2] Department of Geophysics, Stanford University, California, US.

[3] Faculty of Geosciences, Institute of Geology, Mineralogy and Geophysics, Ruhr University Bochum, Bochum, Germany.

[4] Free University Berlin, Institute of Geological Sciences, Berlin, Germany

Corresponding author: Patricia Martínez-Garzón (patricia@gfz-potsdam.de)

Key Points:

- We generated high-resolution micro-seismicity catalogs to investigate an earthquake sequence in a hydrothermal region south of Istanbul.
- Larger seismicity rates are observed shortly after local minima in sea level, during time periods when sea level is increasing.
- Differential strain estimates from local strainmeters suggest that 30 to 300 nstrain was enough to generate seismicity.

Abstract

Small stress changes such as those from tidal loading can be enough to trigger earthquakes. If small and large earthquakes initiate similarly, high resolution catalogs with low detection thresholds are best suited to illuminate such processes. Below the Sea of Marmara section of the North Anatolian Fault, a segment of ≈150 km is late in its seismic cycle. We generated high-resolution seismicity catalogs for a hydrothermal region in the eastern Sea of Marmara employing both AI-based and template matching techniques to investigate a complex long-lasting sequence including seismicity up to M_W 4.5. We document a strong effect of the Sea of Marmara level changes on the local seismicity. Both high resolution catalogs show that local seismicity rates are significantly larger during time periods shortly after local minima on sea level. Local strainmeters indicate that the associated strain changes, on the order of 30-300 nstrain, are sufficient to promote seismicity.

Plain summary abstract

Periodic phenomena are a natural probe to test how the Earth's responses to a certain stress perturbation. One of these phenomena are the solid Earth tides, which has been observed to trigger seismicity under selected conditions. High resolution catalogs with low detection thresholds may provide a new opportunity to look for these type of earthquake triggering. A segment of 150 km below the Sea of Marmara section of the North Anatolian Fault is late in its seismic cycle. Here, we generated high-resolution seismicity catalogs for a region in the eastern Sea of Marmara to investigate an earthquake sequence including seismicity up to M_W 4.5 in a hydrothermal region south of Istanbul. For first time in this region, we document a strong effect of the Sea of Marmara level changes on the local seismicity. Both high resolution catalogs show that local seismicity rates are significantly larger during time periods shortly after local minima on sea level. The available local instrumentation allowed to provide an estimate of the strain changes that were sufficient to promote seismicity. Typically, if such small stress perturbations from sea level changes are enough to trigger seismicity, this implies that the fault is very close to failure.

1 Introduction

For decades the Earth's periodic phenomena such as tidal movements or seasonal effects have been studied to investigate whether small, but predictable stress changes are sufficient to trigger regular or low frequency earthquakes (Tanaka et al., 2002; Obara, 2002). The response to a known forcing can provide insight

into the stress change needed to activate faults and hence the probable timing of earthquakes, and more generally to the processes promoting earthquake initiation. Solid-Earth tides can trigger both earthquakes and tectonic tremor. The conditions that promote tremor include elevated pore pressure and low effective normal stresses, and hence triggering of tectonic tremor by solid earth tides has been observed often where ambient tremor occurs, including Nankai (Shelly et al., 2007), Cascadia (Rubinstein et al., 2008), and the creeping portion of the San Andreas transform fault (Thomas et al., 2009; Elst et al., 2016). Tidal triggering of earthquakes is far less common, and has been observed in only few places where the Earth's crust is sufficiently close to failure that small stress changes can induce slip, including shallow thrust faults at global scale (Cochran et al., 2004) and mid-oceanic ridges such as the East Pacific Rise (Stroup et al., 2007). An extreme case of triggered seismicity from periodic changes in the water level comes from the Koyna and Warna hydro-electric power plants (India), where $M > 5$ earthquakes have occurred following the water level increase from the monsoon rains (Bansal et al., 2018; Gupta, 2018). Some models of earthquake nucleation hold that large and small earthquakes begin similarly (Ellsworth & Beroza, 1995; Beroza & Ellsworth, 1996). If small and large earthquakes share a common nucleation process, high resolution earthquake catalogs should better illuminate it.

In the last few years, fast and efficient processing of vast data volumes has been achieved with the emergence and application of artificial intelligence (AI). AI methods are promising for addressing a number of seismological challenges, including enhancement of seismicity catalogues (e.g. Zhu & Beroza, 2019) and opens new opportunities for better capturing physical processes compared with traditional seismicity catalogs, such as the detailed imaging of fault architecture (Ross, 2021) and elucidation of pathways between fluid-injection wells (Park et al., 2020). Such catalogs provide a new opportunity to investigate earthquake triggering processes. However, their properties warrant a thorough evaluation to minimize false detections and interpret the results with confidence. For that reason, it is essential to compare and benchmark results from AI-based seismic catalogs with those obtained with traditional catalogs and other high-resolution well-established techniques such as template matching.

The major plate bounding North Anatolian transform Fault in Türkiye splits into several segments before entering the Sea of Marmara, where it runs within 20 km of metropolitan Istanbul (Fig 1a). That 150-km fault segment last ruptured in a $M > 7$ earthquake 256 years ago. Because the recurrence interval for $M > 7$ earthquakes is approximately 250 years (Parsons, 2004), the fault is considered to be late in its seismic cycle. On the southern shore of the Sea of Marmara, directly south of Istanbul, the Armutlu Peninsula is a hydrothermal region displaying high heat flow and abundant hot springs (Eisenlohr, 1995). The area is rich in crustal fluids likely resulting in elevated pore pressures (Fig 1). Seismic swarms frequently occur, connected with episodic slow slip transients (Martínez-Garzón et al., 2019; Martínez-Garzón et al., 2021). Hydrothermal regions are frequently observed to be sensitive to earthquake triggering, e.g.

following the occurrence of large local or regional earthquakes (Saar & Manga, 2003; Aiken & Peng, 2014). Similarly, the Armutlu Peninsula is sensitive to local stress perturbations from large earthquakes, hosting vigorous aftershock activity following the 1999 M_W 7.4 Izmit earthquake (Durand et al., 2010; Karabulut et al., 2011).

The northern portion of the Armutlu Peninsula (Fig. 1) has been interpreted as a horsetail splay fault structure associated with a major normal fault (Kinscher et al., 2013) and it may have hosted the M 6.3 normal-faulting earthquake in 1963 (Bulut & Aktar, 2007; Pinar et al., 2003). The region also hosted the western termination of the 1999 M_W 7.4 İzmit earthquake rupture (Armijo et al., 2005). In recent years, the northern portion of the Armutlu Peninsula displays one of the highest background seismicity rates in the Sea of Marmara (Wollin et al., 2018; Martínez-Garzón, Ben-Zion, et al., 2019). Two slow deformation transients, possibly related to the shallow part of local normal faults have been observed with strainmeter recordings to occur temporally connected with moderate $M > 4$ local seismic events (Martínez-Garzón et al., 2019; Martínez-Garzón et al., 2021).

We investigated the initiation of a complex earthquake sequence that took place in the northern portion of the Armutlu Peninsula over the course of about two months, including three $M > 4$ seismic events. The largest event, a M_W 4.5 activated an onshore normal fault that also hosted at least three periods of intense seismic activity over the following year (Martínez-Garzón et al., 2021). We generated high-resolution seismicity catalogs using both AI-based and template matching techniques, and compared the results with those from the standard catalogs. Both high-resolution catalogs show that local seismicity rates are larger during the time periods shortly after local minima in the sea level, when the sea level is rising. This correlation is not apparent in the standard catalogs. During that time, data from the local strainmeter BOZ1 reports a minimum and maximum in the areal and differential strain, respectively, suggesting that stress conditions are optimal to trigger seismicity.

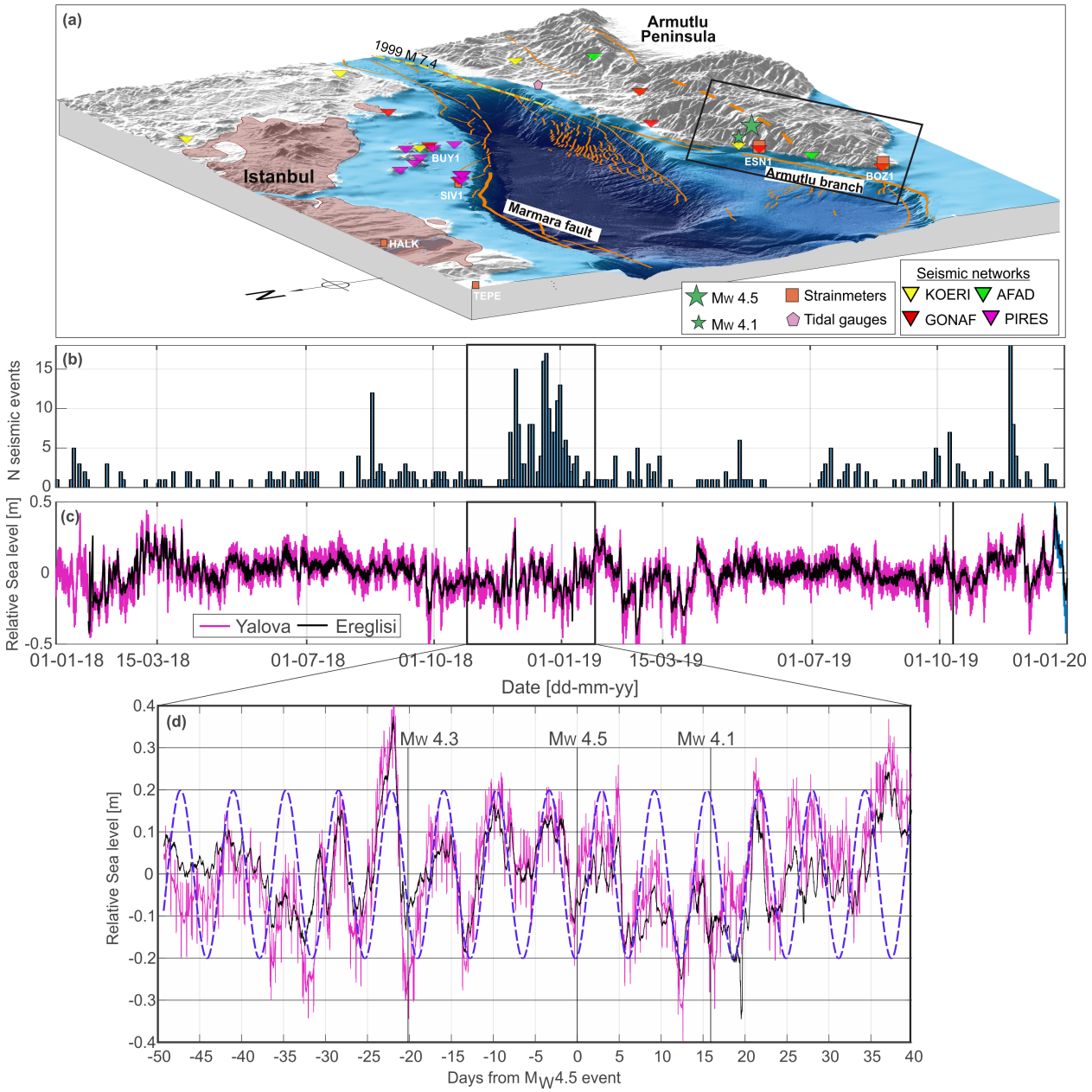

Figure 1: (a) Topography and bathymetry of the eastern Sea of Marmara region. (b) Seismicity rates from a standard catalog (KOERI) shown in two-day bins for northern Armutlu Peninsula from 2018 to 2020. (c) Relative sea level changes from two tidal gauge stations located in Yalova and Ereglisi (magenta and black lines, respectively). In (b) and (c) the black rectangle marks the

analyzed time period. (d) Zoom of the relative sea level changes during the analyzed time period. Dashed blue line is a sinusoidal function with a period of 6.3 days.

2 Data and Methods

We focused on a time window spanning 90 days from Nov 1st, 2018 to Jan 31st, 2019, in the northern Armutlu region (longitude 28.80-29.10, latitude 40.4-40.625) (Fig 1). The region hosted a vigorous seismic sequence, including a M_W 4.1 and a M_W 4.5 earthquakes rupturing a small normal fault. The analyzed time period is the most seismically active from Jan 2018 to Jan 2020 (Fig 1b).

We analyzed time series of tidal gauges from two stations in the towns of Yalova and Ereglisi, providing a measurement every 15 min. The long-term records (2018-2020) show seasonality pattern in that from October to April, sea level displays larger and more rapid variations up to 0.8 m, while from April to September sea level changes are smaller than 0.3 m (Figs 1b, c).

We generated three high-resolution seismicity catalogs employing AI-based and template matching techniques and compared the results with those obtained with the standard catalogs. Common detections between the different datasets are illustrated using Venn diagrams (Fig S1). In the following we describe the individual catalogs. In all catalogs, we assumed $M_L \approx M_W$ for earthquakes with $M_L < 4$ when no M_W was available (Kılıç et al., 2017).

1. Turkish Disaster Management Presidency (AFAD) national seismicity catalog. For the selected time period and region, this catalog is composed of 129 seismic events with M_W in the range [0.9, 4.5].

2. KOERI national seismicity catalog. For the selected time period and region, this catalog is composed of 151 seismic events with M_W in the range 0.8-4.6.

3. Catalog derived utilizing AI-based techniques. We applied the PhaseNet deep learning method (Zhu & Beroza, 2019) to detect and pick the P-and S- waves of seismic events embedded in continuous seismic recordings from 16 stations surrounding the region of interest (Fig S2) resampled at 100 Hz. The method was trained on a dataset from Northern California, but has been shown to generalize well to other tectonic settings. We obtained 323,085 picks, of which 166,963 (51%) are P-wave picks. The picks were associated into seismic events using the GaMMA association method (Zhu et al., 2022). We manually checked waveforms from all detections and 516 seismic events with visually clear waveforms were retained. We estimated their location using the non-linear earthquake location algorithm NLLoc (Lomax et al., 2000) and the velocity model from Bulut et al., (2009). The locations of the final 390 events for which five or more stations were available are provided in Fig S3.

4. Template matching catalog A. We applied the matched filter algorithm EQcorrscan (Chamberlain et al., 2017) to the two nearby seismic stations with the largest data recovery during the period of interest, ARMT and MDNY (Fig S2). Details on this catalog are included in Supp Text S1. This catalog contains 2,462 seismic events (all manually reviewed) with magnitudes M_W in the range [-2.4, 4.5]. Because of the inclusion of only two stations, independent location of these events is not possible.

5. Template matching catalog B. We derived a second template matching catalog utilizing twelve of the closest seismic stations displaying high seismic data recovery during the analyzed time period (Fig S2). An initial list of detections was generated following the same steps as for the Template Matching Catalog A, with the additional requirement that all detections must contain at least one picks from one of the two closest stations, ARMT and MDNY. All detections from this catalog were also manually reviewed. For events with more than 5 picks, we estimated their location using the non-linear algorithm NLLoc (Lomax et al., 2000) and the velocity model from (Bulut et al., 2009). This catalog includes 717 seismic events with magnitudes M_W in the range [-2.1, 4.5] (Fig S4).

The eastern Sea of Marmara region hosts six Gladwin tensor borehole strainmeters (150 m depth) at different locations deployed by UNAVCO (Fig 1a) and five of these were operating during the time period analyzed. The closest two to the M_W 4.5 earthquake are located at 5.5 km and 22 km distance near the villages of Esenkoy (ESN1) and Armutlu (BOZ1), respectively. Both are part of the Geophysical borehole Observatory at the North Anatolian Fault (GONAF, Bohnhoff et al., 2017, Fig. 1a). Processing of strainmeter data is performed by UNAVCO and includes down sampling from 300 to 1 sps to simplify data handling. Tidal corrections and borehole trends were applied to the strainmeter recordings following (Hodgkinson et al., 2013). Corrections for the M2 (the largest lunar constituent) and O1(lunar diurnal) tidal modes are calculated using the SPOTL (Agnew, 1996) tidal program and subtracted from each gauge. The correction of the borehole relaxation trend is calculated by fitting exponential functions to the raw data from the four different gauges of the strain tensor during the entire time of data acquisition. From these corrected we calculated the areal ε_{N+E}, differential ε_{E-N} and engineering $2\varepsilon_{\mathrm{EN}}$ strain components as:

$$\begin{aligned} \varepsilon_{N+E} &= \varepsilon_{\mathrm{EE}} + \varepsilon_{\mathrm{NN}} \\ \varepsilon_{E-N} &= \varepsilon_{\mathrm{EE}} - \varepsilon_{\mathrm{NN}} \quad [1] \\ 2\varepsilon_{\mathrm{EN}} &= \varepsilon_{\mathrm{EN}} + \varepsilon_{\mathrm{NE}} \end{aligned}$$

where $\varepsilon_{\mathrm{EE}}$, $\varepsilon_{\mathrm{NN}}$ and $\varepsilon_{\mathrm{EN}}$ are the three independent components of the horizontal strain tensor and the symmetry condition $\varepsilon_{\mathrm{EN}} = \varepsilon_{\mathrm{NE}}$ applies. We focus on the areal strain, ε_{N+E}, which is more sensitive to changes in the water column, as well as the differential strain, ε_{E-N}, which is more sensitive to tectonic

deformation.

3 Results and discussion

3.1 Seismicity rates modulated by sea level

The most prominent sea level change during the analyzed time period can be approximated by a sinusoidal function with a period of T = 6.3 days (Fig 1d), related to the fortnightly solid-Earth tides. During the last 20 days, however, the sea level changes did not follow that sinusoidal function. The amplitude of the sea level change typically did not exceed $\pm 0.2m$, except on day -20 relative to the M_W 4.5 event, when seismicity rates increased including a M_W 4.1 earthquake shortly after a sea level decrease of -0.6 m, which was the largest observed sea level change (Fig 1c).

All M_W 4.1, 4.5, and 4.3 earthquakes occurred shortly after local minima of the sea level (Fig 1d, Fig 2). The five seismicity catalogs have very different magnitude detection thresholds, but the daily seismicity rates follow a similar distribution for each (Fig 2). Almost no seismic events were detected during the first 20 days (-50 to -30) in any of the catalogs. A small number of seismic events are present in the catalogs from day -28. Around day -20, after a local minimum in sea level the seismicity rates increased, including a M_W 4.1 event. Rather than dying out as a classical aftershock sequence, seismicity continued until day 0, when enhanced seismicity rates following another local minimum in the sea level culminated in the M_W 4.5 mainshock that ruptured the same onshore fault as the previous M_W 4.1 event. Between days 0 and 16, seismicity rates were the highest in the observed period, until the occurrence of the M_W 4.3 event in a perpendicular structure offshore. After the occurrence of this event, seismicity rates decayed, with only one more period of elevated seismicity after a local minimum of the sea level (day 25) (Fig 2).

We investigated whether seismicity rates were affected by the phase of the sea level cycle. We assigned a phase of $\theta = 0, 360^\circ$ and θ =180 to each of the local sea level maxima and minima, respectively, so that phase values in the range [0-180] correspond to sea level decrease and values in the range [180-360] represent periods of sea level increase (Fig 3a, Fig S5). We evaluated the statistical significance of the observation of seismicity rates depending on sea level by applying a Schuster test (e.g. Cochran et al., 2004; Shelly et al., 2007). For the three high-resolution catalogs, without the aftershock sequences of the largest events (see description below), the probability that the seismic events occur independently of the sea level phase (p-value) is smaller than 1%. In contrast, for the two standard catalogs the p-values are approximately 1% or slightly larger. Therefore, high-resolution catalogs strongly support the notion that the events are triggered by sea level changes.

The three high resolution catalogs unambiguously show that seismicity rates are larger during the periods of sea level increase, where the increase in the

water body should increase the stress loading (Figs 3b-d). All three catalogs show a peak in the seismicity rates for $\theta \approx 200^{\circ}$, shortly after local minima, and a second peak around $\theta \approx 330^{\circ}$. With the standard seismicity catalogs, the limited number of events would not have allowed a firm conclusion (Figs 3e, f).

The selected time range included two earthquakes with magnitudes M_W 4.5 and M_W 4.1 that generated their own aftershock sequences, we removed from the analysis all seismicity during the three and two subsequent days following the M_W 4.5 and 4.1 mainshocks, respectively. These time ranges were selected based on the distribution of the number of events with respect to time, which decays following Omori's law within those time periods (Fig S6). It is not necessary to remove seismicity after the M_W 4.3 event as no aftershock sequence is observed (see e.g. Fig 2). In the high-resolution catalogs, the difference in seismicity rates between the tidal phases is maintained, although the peak of the distributions at $\theta \approx 200^{\circ}$ is considerably reduced. This is mainly because both M_W 4.5 and M_W 4.1 events occurred shortly after the local minimum of the sea level, and therefore the aftershock sequences mainly occurred during the initial phase of the sea level increase (Fig 3).

Another common source of periodicity in the seismicity rates is a difference between the day and night hours. Seismicity catalogs tend to display larger number of events during the night hours due to the decreased noise. We observe such effect in our three high-resolution catalogs (Fig S7), but this variation is much less prominent than that between the seismicity and the sea level. The semi-diurnal tides are marginally observable in the tide-gauge time series, while the fortnightly cycle is prominent (e.g. Fig 1d).

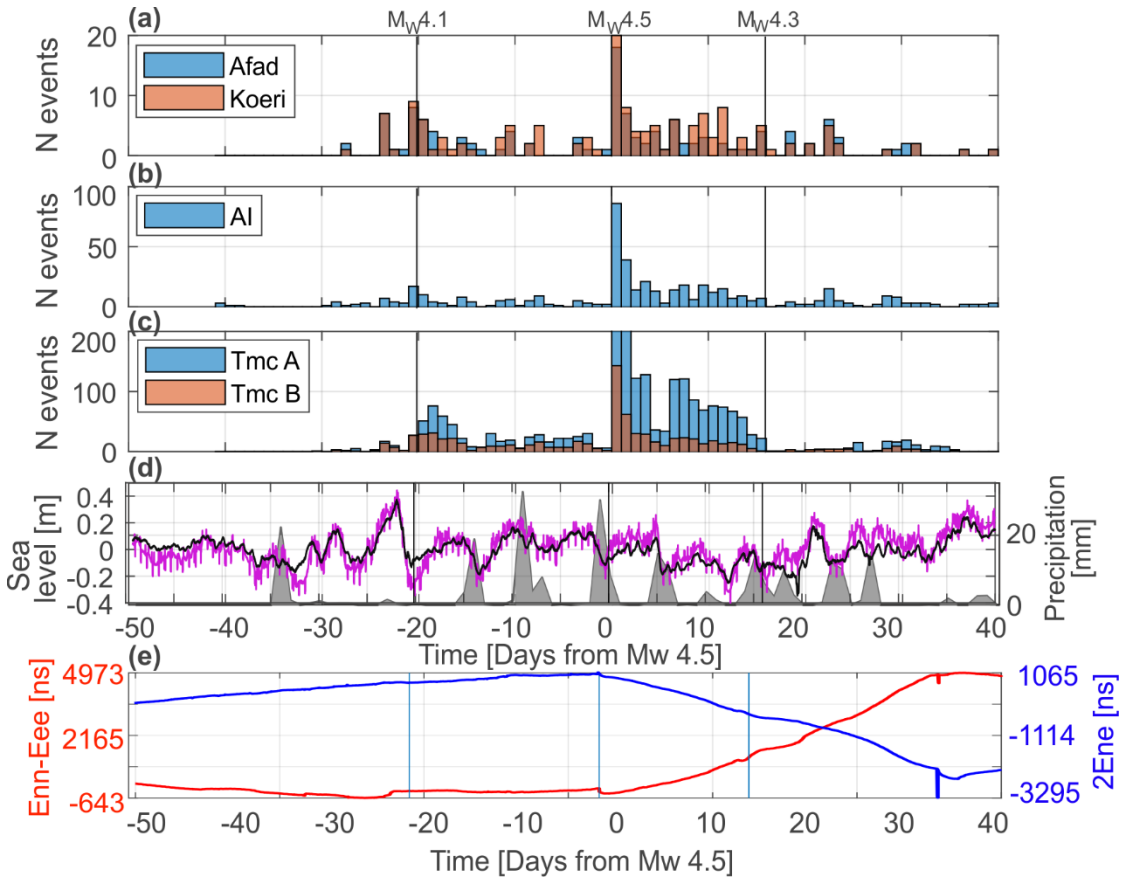

Figure 2: Evolution of daily seismicity rates for the seismicity catalogs and relation to the sea level, precipitation and slow slip. (a) Seismicity rates from AFAD and KOERI catalogs, (b) Seismicity rates from the catalog derived with AI-based techniques, (c) Seismicity rates derived with two template matching catalogs utilizing different number of stations (see Data and Methods for details). (d) Sea level from the Yalova and Ereglisi stations (magenta and black lines, respectively). Precipitation data from a pluviometric station in Yalova is represented with grey filled shapes. (e) Evolution of differential and engineering strain (red and blue lines, respectively) from BOZ1 strainmeter. A slow transient can be observed starting in day 0 (see Martínez-Garzón et al., 2021 for details).

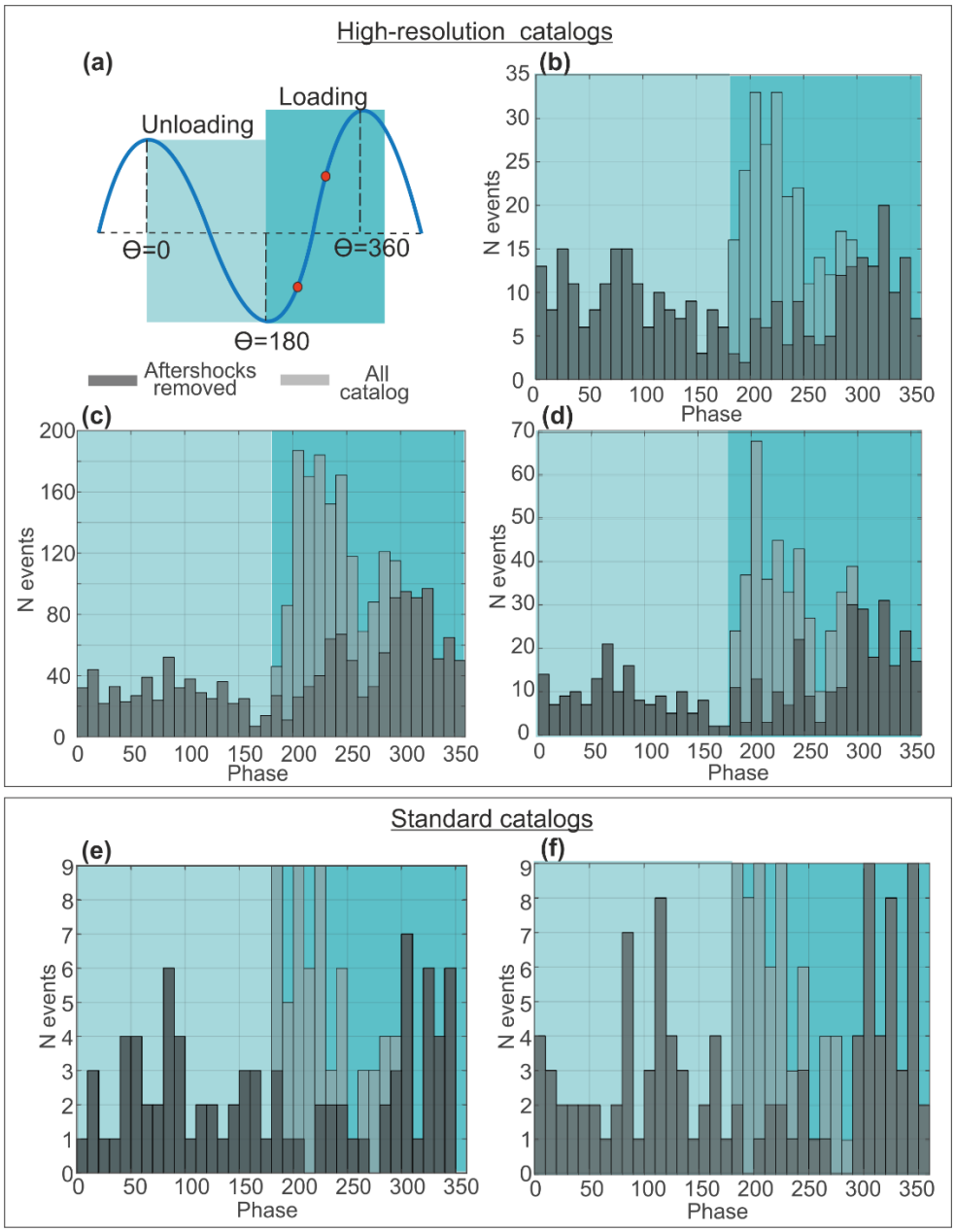

Figure 3: (a) Conceptual sketch illustrating the phases assigned to the observed sea level changes following a period of T=6.3 days. Light and darker blue turquoise colors differentiate the phases that represent a sea level increase and decrease. (b) Number of seismic events with respect of the sea level phase employing the seismicity

catalog derived with AI techniques. (c, d) Same as (b) but for the template matching catalogs A and B. (e, f) Same as (b) but employing the standard seismicity catalogs from the national agencies AFAD and KOERI, respectively. In all plots, light grey bars represent the statistics utilizing the entire catalogs, while dark grey bars represent the seismicity catalogs once that aftershock sequences from the three largest events have been removed.

3.2 Constraining strain changes from sea level movement

The temporal evolution of the areal strain ε_{N+E} tracks the evolution of the sea level (Fig. 4a, Fig S8) as expected because ε_{N+E} as the trace of the horizontal strain tensor is more sensitive to vertical loading and unloading than the shear strain components. Between Days -25 and -20 (containing the largest sea level change and immediately before the M_W 4.1 earthquake), we observe a change in ε_{N+E} of about -100, -700 and -100 nstrain in ESN1, BOZ1 and BUY1, respectively (Fig 4a). During that time, the change in the sea level was about $z = 0.6\ m$. Therefore, the pressure change from the change in the water column would be approximately $P = \rho g\ z = 16\ kPa$. The geological units in which the ESN1 and BOZ1 strainmeters are deployed are amphibolites and serpentinites, respectively (Eisenlohr, 1995). Assuming a Young's modulus of $E = 60\ GPa$ for these rocks, we can estimate the strain change from the change in the water column as $\in = \frac{P}{E} = 266\ nstrain$, which is of the same order as observed. The relation between the differential strain ε_{E-N} and the sea level is less obvious, because this component is more sensitive to shear strain changes, but some response is also observed during the largest sea water changes (Fig 4b, Fig S8). The change in ε_{E-N} between the Days -25 and -20 is approximately 60, 300 and 30 nstrain for ESN1, BOZ1 and BUY1, respectively. The differences in strain values recorded by the different strainmeters could be due to several local effects, including poroelastic effects, or the coupling between the instrument and the surrounding medium. This was well illustrated with the strong differences obtained between the modelled and observed coseismic strain offsets from the occurrence of several earthquakes in southern California (Barbour, 2015).

Estimating the average areal and differential strain components of the BOZ1 strainmeter over all tidal cycles shows that the areal ε_{N+E} (representing a normal strain) component reaches a minimum around θ =180-200. Simultaneously, the differential component ε_{E-N} (representing a shear strain) reaches a maximum value around θ =200 (Fig 4c, d). Hence, the ratio between the shear to normal strain promoting failure should be the largest around θ =200, which is in good agreement with the largest peak in the seismicity rates that we observe with the entire catalog (Fig 3). This is also in agreement with previous observations of earthquake triggering from tidal loading, where shallow thrust faults were brought to slip when the Coulomb stress from the tidal movement was at its peak (Cochran et al., 2004). However, we note that the standard deviation of the strain changes over the tidal cycle are larger, and therefore the

strain change is within the uncertainties of the strainmeter fluctuations. Recent experiments on laboratory rock samples subjected to periodic loading shown that rates of acoustic emissions were promoted during periods of pore pressure decrease (Chanard et al., 2019). As the faults that we observed to be seismically active during our analysis are mainly onshore, tracking the evolution of the pore pressure changes in the system with respect to tidal cycles is not trivial and therefore our observations cannot be directly compared.

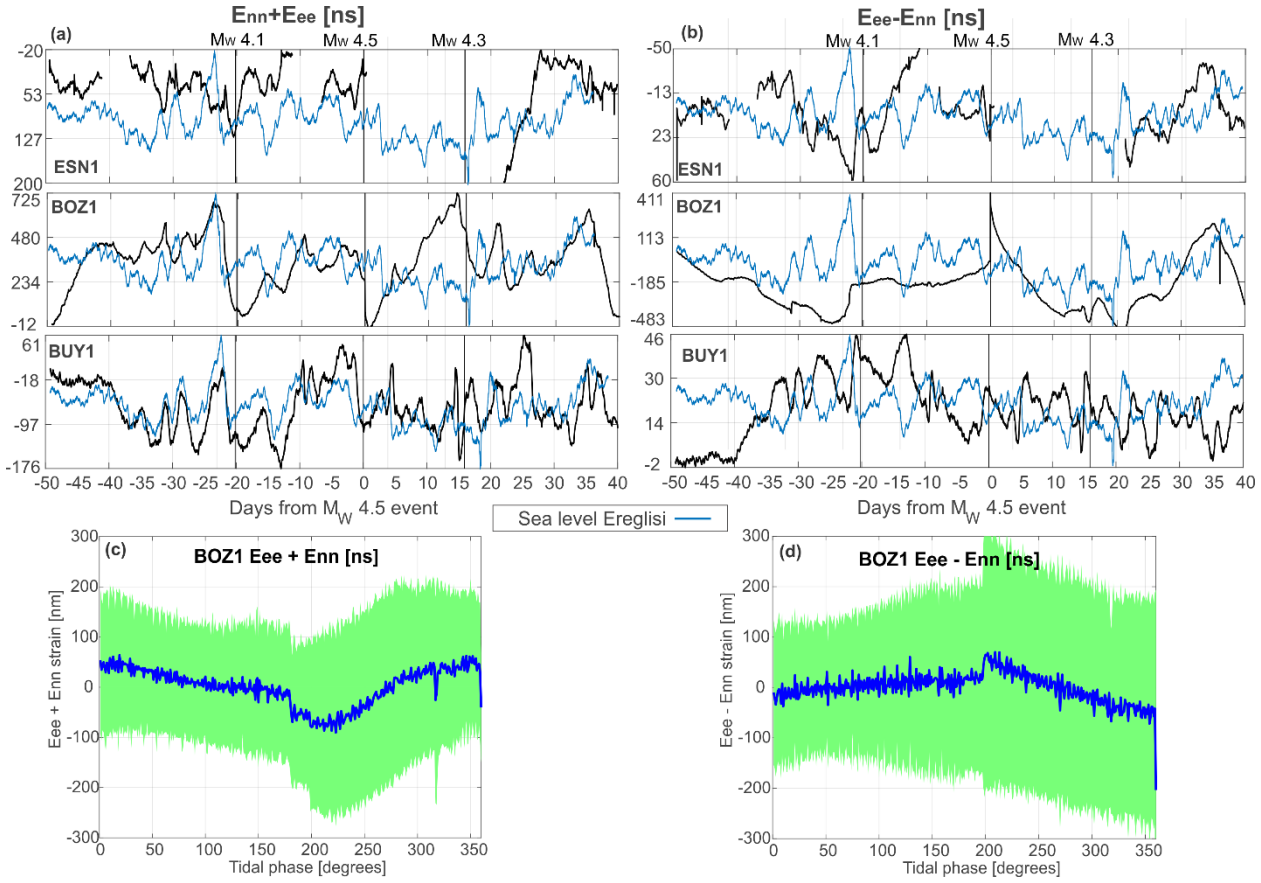

Figure 4: Evolution of areal strainmeter components (a) and differential strain components (b) during the analyzed time period (ordered from top to bottom according to distance to the M_W 4.5 event). Blue line represents the sea level evolution as recorded by Ereglisi station (for units, see Fig. 2). Vertical black lines mark the origin time of the M_W 4.1, M_W 4.5 and M_W 4.3 events that occurred within the study region. (c) areal strain component from strainmeter BOZ1 with respect to tidal phase average over all cycles of the analyzed time period (blue line), together with its standard deviation (green area). (d) Same as (c) but for the differential strain component.

4 Conclusions

We investigated the relation between sea level changes and the evolution of a sequence of moderate seismicity in a hydrothermal system in the Sea of Marmara region, Turkey, over the course of three months. We generated high-resolution seismicity catalogs using both AI-based and template matching techniques, and compared their results with standard catalogs employing traditional techniques. Both high-resolution catalogs showed that local seismicity rates significantly increased during periods when sea level is increasing (including the three largest events up to M_W 4.5), which was not apparent in the standard catalogs.

Recordings from nearby borehole strainmeters documented that during the sea level phase $\theta = 200^\circ$, shortly after the minimum, the areal and differential strains reach minimum and maximum values, respectively, thus contributing to local fault unclamping and activation, although the standard deviation of the strain measurements is large and the strain change is within the associated uncertainties.

The relatively short analyzed time window covering three months provides insight in the possible role of sea level changes on the state of stress of the faults in the eastern Marmara region. Subsequent analysis of longer time periods will be needed to investigate whether this observation holds, or if this observation is representative of a short time window within the seismic cycle.

Acknowledgments

P.M.G. acknowledges funding from the Helmholtz Association in the frame of the Young Investigators Group VH-NG-1232 (SAIDAN). G.C.B. was supported by research award from the Alexander von Humboldt Foundation. G.M.B. was partially supported through the VW momentum grant awarded to R.M.H. We thank Murat Nurlu for discussions and collaboration within the ICDP-GONAF borehole network.

Open Research

Seismicity catalogs generated in this study with Artificial intelligence and template matching techniques are being prepared for public release through the repository of the GFZ Data Services (link in preparation). While the data publication gets ready, we provide the three catalogs developed here including detection time of the events within the submission files.

Seismicity catalogs from AFAD and KOERI agencies are available under the landing websites https://tdvms.afad.gov.tr/ (last accessed 05/08/2022) and http://www.koeri.boun.edu.tr/sismo/2/earthquake-catalog/ (last accessed 05/08/2022), respectively. The here generated AFAD and KOERI catalogs correspond to the time period from Nov 1st, 2018 to Jan 31st, 2019, and longitude and latitude ranges of 28.80°-29.10°, and 40.4°-40.625°, respectively.

References

Agnew, D. C. (1996), SPOTL: Some programs for ocean-tide loading, SIO Ref. Ser. 96-8, 35 pp., Scripps Institution of Oceanography, La Jolla, CA

Aiken, C., & Peng, Z. (2014). Dynamic triggering of microearthquakes in three geothermal/volcanic regions of California. *Journal of Geophysical Research: Solid Earth*, *119*(9), 6992–7009. https://doi.org/10.1002/2014JB011218

Armijo, R., Pondard, N., Meyer, B., Uçarkus, G., de Lépinay, B. M., Malavieille, J., et al. (2005). Submarine fault scarps in the Sea of Marmara pull-apart (North Anatolian Fault): Implications for seismic hazard in Istanbul. *Geochemistry, Geophysics, Geosystems*, *6*(6), Q06009. https://doi.org/10.1029/2004GC000896

Bansal, A. R., Rao, N. P., Peng, Z., Shashidhar, D., & Meng, X. (2018). Remote Triggering in the Koyna-Warna Reservoir-Induced Seismic Zone, Western India. *Journal of Geophysical Research: Solid Earth*, *123*(3), 2318–2331. https://doi.org/10.1002/2017JB014563

Barbour, A. J. (2015). Pore pressure sensitivities to dynamic strains: Observations in active tectonic regions. *Journal of Geophysical Research: Solid Earth*, *120*(8), 2015JB012201. https://doi.org/10.1002/2015JB012201

Beroza, G. C., & Ellsworth, W. L. (1996). Properties of the seismic nucleation phase. *Tectonophysics*, *261*(1), 209–227. https://doi.org/10.1016/0040-1951(96)00067-4

Bohnhoff, M., Dresen, G., Ceken, U., Kadirioglu, F. T., Kartal, R. F., Kilic, T., et al. (2017). GONAF-the borehole Geophysical Observatory at the North Anatolian Fault in the eastern Sea of Marmara. *Scientific Drilling*, *5*, 1–10.

Bulut, F., & Aktar, M. (2007). Accurate relocation of İzmit earthquake (Mw = 7.4, 1999) aftershocks in Çınarcık Basin using double difference method. *Geophysical Research Letters*, *34*(10), n/a-n/a. https://doi.org/10.1029/2007GL029611

Bulut, F., Bohnhoff, M., Ellsworth, W. L., Aktar, M., & Dresen, G. (2009). Microseismicity at the North Anatolian Fault in the Sea of Marmara offshore Istanbul, NW Turkey. *Journal of Geophysical Research: Solid Earth*, *114*(B9), B09302. https://doi.org/10.1029/2008JB006244

Chamberlain, C. J., Hopp, C. J., Boese, C. M., Warren-Smith, E., Chambers, D., Chu, S. X., et al. (2017). EQcorrscan: Repeating and Near-Repeating Earthquake Detection and Analysis in Python. *Seismological Research Letters*, *89*(1), 173–181. https://doi.org/10.1785/0220170151

Chanard, K., Nicolas, A., Hatano, T., Petrelis, F., Latour, S., Vinciguerra, S., & Schubnel, A. (2019). Sensitivity of Acoustic Emission Triggering to Small Pore Pressure Cycling Perturbations During Brittle Creep. *Geophysical Research Letters*, *46*(13), 7414–7423. https://doi.org/10.1029/2019GL082093

Cochran, E. S., Vidale, J. E., & Tanaka, S. (2004). Earth Tides Can Trigger Shallow Thrust Fault Earthquakes. *Science*, *306*(5699), 1164–1166. https://doi.org/10.1126/science.1103961

Durand, V., Bouchon, M., Karabulut, H., Marsan, D., Schmittbuhl, J., Bouin, M.-P., et al. (2010). Seismic interaction and delayed triggering along the North Anatolian Fault. *Geophysical Research Letters*, *37*(18). https://doi.org/10.1029/2010GL044688

Eisenlohr, T. (1995). Die Thermalwasser der Armutlu-Halbinsel (NW-Turkei) und deren Beziehung zu Geologie und aktiver Tektonik. ETH Zurich (PhD Thesis).

Ellsworth, W. L., & Beroza, G. C. (1995). Seismic Evidence for an Earthquake Nucleation Phase. *Science*, *268*(5212), 851–855. https://doi.org/10.1126/science.268.5212.851

Elst, N. J. van der, Delorey, A. A., Shelly, D. R., & Johnson, P. A. (2016). Fortnightly modulation of San Andreas tremor and low-frequency earthquakes. *Proceedings of the National Academy of Sciences*, *113*(31), 8601–8605. https://doi.org/10.1073/pnas.1524316113

Gupta, H. K. (2018). Review: Reservoir Triggered Seismicity (RTS) at Koyna, India, over the Past 50 Yrs. *Bulletin of the Seismological Society of America*, *108*(5B), 2907–2918. https://doi.org/10.1785/0120180019

Hodgkinson, K., Langbein, J., Henderson, B., Mencin, D., & Borsa, A. (2013). Tidal calibration of plate boundary observatory borehole strainmeters. *Journal of Geophysical Research: Solid Earth*, *118*(1), 447–458. https://doi.org/10.1029/2012JB009651

Karabulut, H., Schmittbuhl, J., Özalaybey, S., Lengliné, O., Kömeç-Mutlu, A., Durand, V., et al. (2011). Evolution of the seismicity in the eastern Marmara Sea a decade before and after the 17 August 1999 Izmit earthquake. *Tectonophysics*, *510*(1–2), 17–27. https://doi.org/10.1016/j.tecto.2011.07.009

Kinscher, J., Krüger, F., Woith, H., Lühr, B. G., Hintersberger, E., Irmak, T. S., & Baris, S. (2013). Seismotectonics of the Armutlu peninsula (Marmara Sea, NW Turkey) from geological field observation and regional moment tensor inversion. *Tectonophysics*, *608*, 980–995. https://doi.org/10.1016/j.tecto.2013.07.016

Kılıç, T., Ottemöller, L., Havskov, J., Yanık, K., Kılıçarslan, Ö., Alver, F., & Özyazıcıoğlu, M. (2017). Local magnitude scale for earthquakes in Turkey. *Journal of Seismology*, *21*(1), 35–46. https://doi.org/10.1007/s10950-016-9581-9

Lomax, A., Virieux, J., Volant, P., & Berge-Thierry, C. (2000). Probabilistic earthquake location in 3D and layered models. In Thurber, C.H. & N. Rabinowitz (Eds.), *Advances in seismic event location* (pp. 101–134). Kluwer, Amsterdam: Springer, Dordrecht. https://doi.org/https://doi.org/10.1007/978-94-015-9536-0_5

Martínez-Garzón, P., Ben-Zion, Y., Zaliapin, I., & Bohnhoff, M. (2019). Seismic clustering in the Sea of Marmara: Implications for monitoring earthquake processes. *Tectonophysics*, *768*, 228176. https://doi.org/10.1016/j.tecto.2019.228176

Martínez-Garzón, P., Bohnhoff, M., Mencin, D., Kwiatek, G., Dresen, G., Hodgkinson, K., et al. (2019). Slow strain release along the eastern Marmara region offshore Istanbul in conjunction with enhanced local seismic moment release. *Earth and Planetary Science Letters*, *510*, 209–218. https://doi.org/10.1016/j.epsl.2019.01.001

Martínez-Garzón, P., Durand, V., Bentz, S., Kwiatek, G., Dresen, G., Turkmen, T., et al. (2021). Near-Fault Monitoring Reveals Combined Seismic and Slow Activation of a Fault Branch within the Istanbul–Marmara Seismic Gap in Northwest Turkey. *Seismological Research Letters*. https://doi.org/10.1785/0220210047

Obara K (2002) Nonvolcanic deep tremor associated with subduction in southwest Japan. Science 296(5573):1679–1681.

Park, Y., Mousavi, S. M., Zhu, W., Ellsworth, W. L., & Beroza, G. C. (2020). Machine-Learning-Based Analysis of the Guy-Greenbrier, Arkansas Earthquakes: A Tale of Two Sequences. *Geophysical Research Letters*, *47*(6), e2020GL087032. https://doi.org/10.1029/2020GL087032

Parsons, T. (2004). Recalculated probability of M 7 earthquakes beneath the Sea of Marmara, Turkey. *Journal of Geophysical Research: Solid Earth*, *109*(B5), B05304. https://doi.org/10.1029/2003JB002667

Pinar, A., Kuge, K., & Honkura, Y. (2003). Moment tensor inversion of recent small to moderate sized earthquakes: implications for seismic hazard and active tectonics beneath the Sea of Marmara. *Geophysical Journal International*, *153*(1), 133–145. https://doi.org/10.1046/j.1365-246X.2003.01897.x

Ross, G. J. (2021). Bayesian Estimation of the ETAS Model for Earthquake Occurrences. *ArXiv:2109.05894 [Physics, Stat]*. Retrieved from http://arxiv.org/abs/2109.05894

Rubinstein, J. L., La Rocca, M., Vidale, J. E., Creager, K. C., & Wech, A. G. (2008). Tidal Modulation of Nonvolcanic Tremor. *Science*, *319*(5860), 186–189. https://doi.org/10.1126/science.1150558

Saar, M. O., & Manga, M. (2003). Seismicity induced by seasonal groundwater recharge at Mt. Hood, Oregon. *Earth and Planetary Science Letters*, *214*(3), 605–618. https://doi.org/10.1016/S0012-821X(03)00418-7

Shelly, D. R., Beroza, G. C., & Ide, S. (2007). Complex evolution of transient slip derived from precise tremor locations in western Shikoku, Japan. *Geochemistry, Geophysics, Geosystems*, *8*(10). https://doi.org/10.1029/2007GC001640

Stroup, D. F., Bohnenstiehl, D. R., Tolstoy, M., Waldhauser, F., & Weekly, R. T. (2007). Pulse of the seafloor: Tidal triggering of microearthquakes at 9°50 N

East Pacific Rise. *Geophysical Research Letters*, *34*(15). https://doi.org/10.1029/2007GL030088

Tanaka S, Ohtake M, Sato H (2002) Evidence for tidal triggering of earthquakes as revealed from statistical analysis of global data. J Geophys Res Solid Earth 107(B10):2211.

Thomas, A. M., Nadeau, R. M., & Bürgmann, R. (2009). Tremor-tide correlations and near-lithostatic pore pressure on the deep San Andreas fault. *Nature*, *462*(7276), 1048–1051. https://doi.org/10.1038/nature08654

Wollin, C., Bohnhoff, M., Martínez-Garzón, P., Küperkoch, L., & Raub, C. (2018). A unified earthquake catalogue for the Sea of Marmara Region, Turkey, based on automatized phase picking and travel-time inversion: seismotectonic implications. *Tectonophysics*. https://doi.org/10.1016/j.tecto.2018.05.020

Zhu, W., & Beroza, G. C. (2019). PhaseNet: a deep-neural-network-based seismic arrival-time picking method. *Geophysical Journal International*, *216*(1), 261–273. https://doi.org/10.1093/gji/ggy423

Zhu, W., McBrearty, I. W., Mousavi, S. M., Ellsworth, W. L., & Beroza, G. C. (2022). Earthquake Phase Association Using a Bayesian Gaussian Mixture Model. *Journal of Geophysical Research: Solid Earth*, *127*(5), e2021JB023249. https://doi.org/10.1029/2021JB023249